Miniaturization and Control of an Unmanned Tiltwing Aircraft

J. Müller [*†], D. Moormann
RWTH Aachen University, Templergraben 55, 52062 Aachen, Germany

ABSTRACT

The objective of this paper is to miniaturize and control an unmanned tiltwing aircraft. For geometric miniaturization and mechanical realization, a lightweight design based on carbon fibre tubes, polystyrene rigid foam and 3D-printed parts is used. The attitude controller is adopted from an existing full-scale tiltwing aircraft and follows the control strategy of Incremental Nonlinear Dynamic Inversion (INDI). The effects of the miniaturization, including low mass inertia combined with comparatively large aerodynamic surfaces, require a re-evaluation of INDI-based assumptions. Due to the aircraft's rear-positioned centre of gravity, the modelled control ability of the main motors has to be adapted and requires special consideration in the controller. The integrity of both, construction and controller, is validated in simulations and flight tests.

1 INTRODUCTION

In drone development the trend of miniaturization is applied particularly on concepts based on multi-rotors [1], fixed-wings [2] and flapping-wings [3]. Aircrafts with transformation and vertical take-off and landing (VTOL) ability, such as tiltwing aircrafts, are usually designed for long range outdoor applications [4, 5] and have not yet been subject to miniaturization.

In this paper, the miniaturization process of a tiltwing aircraft based on an existing tiltwing aircraft with a targeted take-off weight of less than $200\,\mathrm{g}$ and a minimum airspeed of $v = 6\,\mathrm{m/s}$ in wing-borne flight is presented. Hereafter, the miniaturized tiltwing aircraft is referred to as Idefix.

Additionally, an attitude controller based on the control strategy of INDI [6] is implemented. Here, the validity of assumptions concerning the negligibility of specific aerodynamic effects is re-evaluated.

The neglect of the distance between thrust vector and centre of gravity is reviewed and the accuracy of the control ability model is investigated accordingly. A validation of both the aircraft construction and the flight controller is conducted through simulation studies and flight tests.

[*]e-mail address: julian.mueller@fsd.rwth-aachen.de
[†]ORCID: 0000-0002-2404-8004

2 MINIATURIZATION OF THE TILTWING AIRCRAFT

Starting point for the miniaturization is the existing tiltwing aircraft Maverix, which was designed at the Institute for Flight System Dynamics of the RWTH Aachen University and has been subject of research since 2014 [7], see Figure 1. With a wingspan of $b = 1.45\,\mathrm{m}$, a wing area of $S = 0.25\,\mathrm{m}^2$ and an empty weight of $m = 1.9\,\mathrm{kg}$, its minimum airspeed in wing-borne flight is $v = 11\,\mathrm{m/s}$.

The goal of the miniaturization is to build the lightest possible aircraft, while retaining all key functions of Maverix. This especially applies to the transformation ability trough a tiltable wing around the wing quarter line in a range of $\alpha_0 < \sigma < 90^\circ$ with α_0 being the angle of incident in wing-borne flight and 90° being the tilt angle for hover flight. The control devices are also kept identical to Maverix, see Figure 1. Less focus is placed on true to scale miniaturization and identical open-loop flight behaviour of both aircrafts.

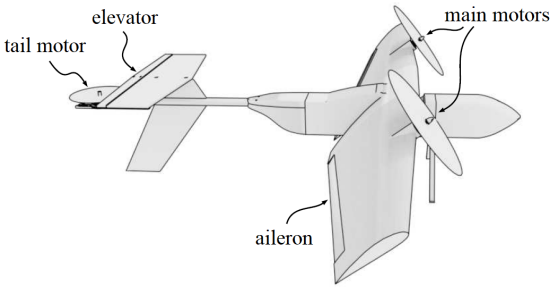

Figure 1: Control devices of Maverix [6]

In addition to requirements for design speed and take-off weight, the following Top Level Aircraft Requirements (TLAR) are set for Idefix:

TLAR		
maximum take-off weight	MTOW	$200\,\mathrm{g}$
minimum speed in wing-borne flight	v_{min}	$6\,\mathrm{m/s}$
minimum flight duration	t_{min}	$5\,\mathrm{min}$
maximum wingspan	b_W	$0.5\,\mathrm{m}$
carrying of a flight computer	m_{fc}	$30\,\mathrm{g}$

Table 1: TLAR for Idefix

For detailed design, Idefix is broken down into following subsystems: propulsion system (1), fuselage (2), wing (3) and tail (4), see Figure 2.

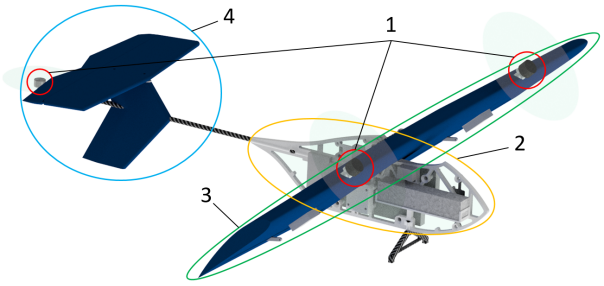

Figure 2: Subsystems of Idefix (CAD)

2.1 Propulsion system design

To ensure sufficient manoeuvrability and provide the capability to carry payload, the combined thrust of the two wing-fixed main motors is set to be at least 1.5 times the aircraft's gravitational force $G_{A/C}$. With a weight of $m = 200\,\mathrm{g}$ this results in a minimum thrust of $F_{M,min} = 1.47\,\mathrm{N}$ per main motor. To increase the efficiency, a motor with low rotation speed and a comparatively large propeller is chosen. A combination of a motor with 4500 revolutions per minute and input voltage (kV) and a $4 \times 2.5\,\mathrm{in}$ propeller, as shown in Figure 3, fulfils these requirements. Powered by a 2S lithium-ion battery with a nominal voltage of $U_N = 7.6\,\mathrm{V}$, this combination delivers a maximum thrust of $F_{M,max} = 1.7\,\mathrm{N}$ with a system mass of $m_M = 7\,\mathrm{g}$.

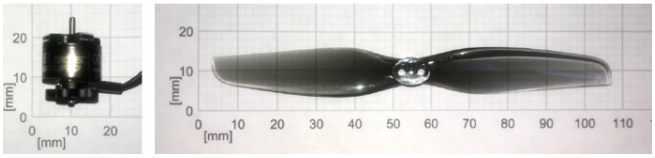

Figure 3: Main motor $(4500\,\mathrm{kV})$ and main propeller $(4 \times 2.5\,\mathrm{in})$

The tail motor is also powered by a 2S lithium-ion battery. It contributes less to the vertical thrust in hover flight and mainly affects the moment equilibrium about the pitch axis. The highest thrust requirement for the tail motor occurs in hover flight configuration, where the absolute value of the main motor and tail motor lever arm ratio becomes minimal with $|\frac{l_T}{l_M}| = 10$. To maintain the pitch moment equilibrium at full main motor thrust, the tail motor needs to deliver a thrust according to Equation 1.

$$F_{T,min} = 2 \cdot F_{M,max} \cdot \left| \frac{l_M}{l_T} \right| = 0.34\,\mathrm{N} \qquad (1)$$

This requirement is met with a combination of a motor with 12000 kV and a $2.5 \times 1\,\mathrm{in}$ propeller, see Figure 4, which yields a thrust of $F_{T,max} = 0.5\,\mathrm{N}$ with a system mass of $m_T = 2.5\,\mathrm{g}$.

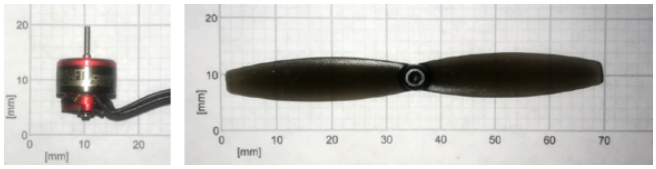

Figure 4: Tail motor (12000 kV) and tail propeller $(2.5 \times 1\,\mathrm{in})$

2.2 Fuselage design

Due to the primarily two-dimensional load on the fuselage consisting of forces in x- and z-direction and moments about the y-axis, the fuselage structure is also chosen to be two-dimensional. To minimise the structural weight and ensure fast reproducibility with a high degree of detail, the structure is 3D-printed in one piece, see Figure 5.

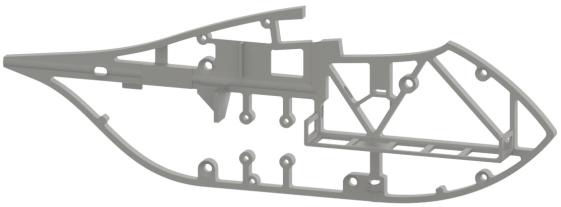

Figure 5: CAD-construction of the fuselage

Besides its function of mechanically connecting all aircraft subsystems, the fuselage also accommodates all main electronic components. Since the available space is limited due to miniaturization, special effort has to be made to ensure electromagnetic compatibility between the electronic components. By splitting the installation space in the symmetry plane via an electromagnetic shielding fleece, the disturbance signal strength of the high-current harness affecting the signal transmission harness can be reduced by up to 100 dB [8, 9], which ensures undisturbed data transmission.

2.3 Wing design

Most conventional design tools like XFLR5 [10] do not consider specific tiltwing effects, such as additional lift produced by higher flow speed at the wing area behind the propeller and tilt of the thrust vector due to the wing's tilt angle. To meet the requirements set in Section 2, an element based simulation developed at the Institute of Flight System Dynamics of the RWTH Aachen University [11], which has been proven to be suitable for the design of tiltwing aircrafts, is used to redesign the wing. For Idefix the same wing profile (NACA 4415) is used as for Maverix, which features both a non-critical stall characteristic and easier lightweight design due to the large profile thickness. The element-based simulation yields, that a wing area of $S_W = 0.05\,\mathrm{m}^2$ is sufficient

for a design speed of $v = 6\,\mathrm{m/s}$ and a angle of incident of $\alpha_0 = 8^\circ$ in wing-borne flight. Fully utilising the required maximum wingspan of $b_W = 0.5\,\mathrm{m}$ and simultaneously attempting to achieve an approximately elliptical lift distribution with easy manufacturability and geometric similarity to Maverix results in a wing geometry according to Figure 6 with a mean chord length of $\bar{t} = 0.1\,\mathrm{m}$.

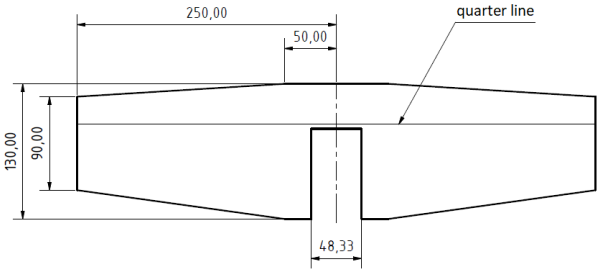

Figure 6: 2D-drawing of the wing [mm]

The lightweight construction of the wing is realised by enforcing a hollow polystyrene structure with a carbon fibre tube. The shielding properties of the carbon fibre can also be taken advantage of by running the data transmission harness inside the tube and the current transmission harness outside, thus resulting in an electromagnetic insulation comparable to the effectivity of the shielding fleece in the fuselage design.

2.4 *Tail and control surface design*

The dimensionless volume coefficients C_h, C_v, C_{ail} and C_{el} are used for scaling the area of the control surfaces of the horizontal stabiliser S_h, the vertical stabiliser S_v, the aileron S_{ail} and the elevator S_{el}, see Equation 2 and 3 [12].

The size and lever arms of Idefix's control surfaces are designed to yield dimensionless volume coefficients identical to Maverix and hence provide sufficient controllability for Idefix. Greater geometrical similarity between both aircrafts is achieved by keeping the aspect ratios of all control surfaces of Idefix as well as the ratio of aircraft width and length identical to those of Maverix.

$$C_h = \frac{S_h \cdot l_h}{S_W \cdot \bar{t}} \;\; ; \;\; C_v = \frac{S_v \cdot l_v}{S_W \cdot b_W} \tag{2}$$

$$C_{ail} = \frac{S_{ail} \cdot l_{ail}}{S_W \cdot b_W} \;\; ; \;\; C_{el} = \frac{S_{el} \cdot l_{el}}{S_W \cdot \bar{t}} \tag{3}$$

The tail structure is kept simple, only consisting of a tail beam made from a carbon fibre tube, which connects both the tail motor and the rear control surfaces with the fuselage, see Figure 7. Analog to the wing, all aerodynamic surfaces are made from polystyrene rigid foam and the insulating effect of the carbon fibre tube is used to minimise electromagnetic interference.

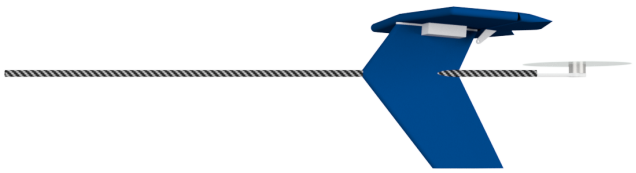

Figure 7: CAD-Construction of the tail

2.5 *Mass properties*

Through consequent lightweight construction, an empty weight of $m = 175\,\mathrm{g}$ can be achieved for the fully assembled Idefix, which is more than 10 times lighter than Maverix. The approximated mass inertia tensor, see Equation 4, is about 100 times lower than that of Maverix. The non-diagonal elements I_{xy}, I_{xz} and I_{zy} as well as changes due to the variable tilt angle of the main wing are negligible and therefore not considered.

$$I = \begin{bmatrix} 884.39 & 0 & 0 \\ 0 & 1456.38 & 0 \\ 0 & 0 & 2160.97 \end{bmatrix} \cdot 10^{-6}\, kgm^2 \tag{4}$$

The approximate coordinates of the centre of gravity are $x_{cg} = -61\,\mathrm{mm}$, $y_{cg} = 0\,\mathrm{mm}$ and $z_{cg} = 19.5\,\mathrm{mm}$, measured from the wing tip in wing-borne flight position in body-fixed coordinates. It is located behind the neutral point and therefore, combined with the low mass inertia, results in higher requirements for the controller compared to Maverix, as is discussed later. In wing-borne flight, the rear-positioned centre of gravity goes along with higher lift demand at the horizontal stabiliser and lower lift demand at the main wing. Thus the required lift can be generated at lower airspeeds.

3 CONTROLLING OF IDEFIX

For the flight controller, the principle of INDI is applied. The theory of INDI is not repeated here and can be found in [6, 13, 14]. By keeping up the central assumption that changes of moments and forces through control devices are much greater than changes of the aerodynamic moments of the aircraft, which in literature is referred to as *time scale separation principle* [15], the control law can be written as follows [6]:

$$u = u_0 + \Delta u = u_0 + B^{-1} \cdot I \cdot (\nu - \dot{\omega}_0). \tag{5}$$

Here, u is the control device command at a certain time step, u_0 the control device command from the previous time step and B^{-1} the pseudo-inverse [16] of the control ability matrix B, which is not directly invertible due to the aircraft's over-actuation [13]. The quantities ν and $\dot{\omega}_0$ represent the pseudo-control input for the INDI controller, which is a vector of commanded angular accelerations and the angular acceleration from the previous time step, respectively. The

closed loop INDI controller following Equation 5 is shown in Figure 8 [6]. Here, $\hat{A}$ is the model of the real control device dynamic A and $\hat{B}$ the model of the real control ability B.

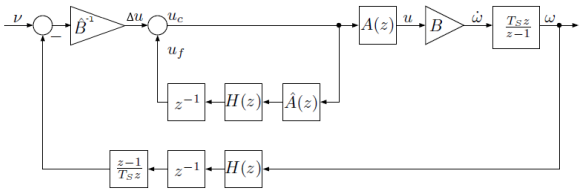

Figure 8: Closed loop INDI Controller [6]

Even though the controller is robust against errors in control ability modelling, the control quality benefits from an accurate modelling of both the control abilities and the control device dynamics. For a more detailed description of the INDI Controller, see [6].

3.1 Control ability

Whereas the control ability for asymmetric thrust, tail motor, ailerons and elevator can be adopted from Maverix [13], the neglect of the pitch effect due to symmetric thrust has to be re-evaluated. This neglect is valid for Maverix because the distance between thrust vector F_M and centre of gravity is small. Thus, the resultant pitch ability B_M, which is equivalent to the change of moment through change of the main motor throttle signal $\frac{\partial M_M}{\partial \delta_M}$, is significantly lower than the tail motor pitch ability B_T. For Idefix, the centre of gravity is located further behind the tilt axis. The pitch ability of the main motors with the kinematic correlation shown in Figure 9 can be described with Equation 6, 7 and 8.

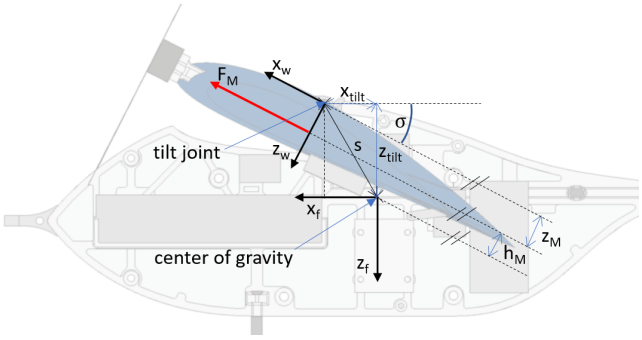

Figure 9: Kinematic correlation of the pitch ability generated by the main motors

$$B_M = \frac{\partial M_M}{\partial \delta_M} = \frac{\partial F_M}{\partial \delta_M} \cdot h_M(\sigma) \tag{6}$$

$$h_M = \sin(90\,^\circ - \arctan\left(\left|\frac{x_{tilt}}{z_{tilt}}\right|\right) - \sigma) \cdot s - z_M \tag{7}$$

$$s = \sqrt{x_{tilt}^2 + z_{tilt}^2} \tag{8}$$

Here, the index w represents the wing-fixed coordinate system [13] with origin in the tilt joint and f the aircraft-fixed coordinate system with origin in the center of gravity. The parameters x_{tilt} and z_{tilt} describe the horizontal and vertical distance between the origins of those coordinate systems, z_M is the orthogonal distance between the thrust vector and the origin of the wing-fixed coordinate system and h_M the effective lever arm between the thrust vector and the origin of the aircraft-fixed coordinate system.

This effect depends on the current tilt angle σ and is maximal in hover flight, where its pitch ability amounts to approximately 33 % of the pitch ability of the tail motor. It contributes much more to the pitch moment equilibrium than it does for Maverix and thus it has to be investigated if the pitch ability needs to be considered in the modelled control ability.

3.2 Consideration of the additional control ability

An alternative approach for calculating the control device commands is replacing the pseudo-inverse from Equation 5 with an optimization algorithm (allocator), which is also used for Maverix [6]. It allows for the prioritization of individual control devices as well as their limitations and hence offers more adjustment options, resulting in more suitable control device commands for the aircraft.

The simplest way to consider the additional pitch control ability is adding it to the existing control ability matrix B, yielding an expanded control ability matrix B_{exp}, see Figure 10.

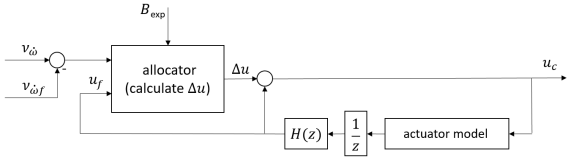

Figure 10: Calculation of the changes of the control device commands by an allocator [6]

Another approach is not considering the additional pitch ability as a control ability but as a predictable disturbing effect with the disturbing ability $B_{M,dist}$. In this case, the original control ability matrix B remains unaltered and the disturbing effect caused by the disturbing ability $B_{M,dist}$ is equalised by adding a tail motor command $\Delta u_{T,add}$ to the previously calculated tail motor command, with Δu_T being the change of the main motor command and B_T being the control ability of the tail motor, see Figure 11 and Equation 9.

$$\Delta u_{T,add} = \Delta u_M \cdot \frac{B_{M,dist}}{B_T} \tag{9}$$

Even though this case avoids using the allocator to find an optimal solution for the control device commands by considering all control abilities, it serves as an alternative approach for compensating the main motor pitch ability. Its effect on the pitch behaviour is analysed in the next section.

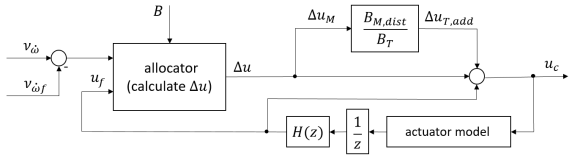

Figure 11: Consideration of the main motor pitch ability as a disturbing effect

4 Validation

The validation of the controller is conducted in both simulation and free flights. An element-based approach implemented in MATLAB/Simulink is used for the simulation [11]. Despite the aim for indoor applicability, the flight tests are executed on an airfield for safety reasons.

4.1 Simulation

For the simulative validation of the attitude controller, the step responses to commanded changes in the reference variables ϕ, θ and $\dot{\psi}$ are investigated. Figure 12 shows the results in hover flight, with a rise time of $1\,\mathrm{s} < t_r < 2\,\mathrm{s}$ and a settling time of $t_s < 3\,\mathrm{s}$ in all axis. The response behaviour is overall stable and comparable to that of Maverix [13].

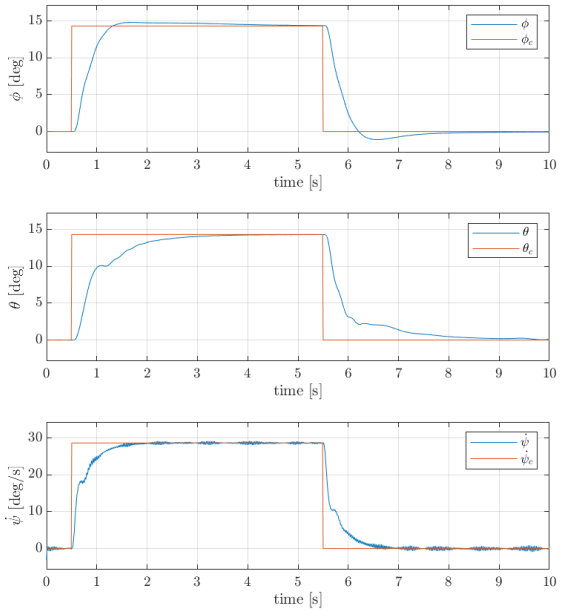

Figure 12: Step response of the attitude controller in hover flight (simulation)

In wing-borne flight, the step response shows similar results in roll and pitch axis, with a slightly higher rise time and an overshoot of less than $2\,^\circ$, see Figure 13. The response in the yaw axis only yields an initial rise of $50\,\%$ and does

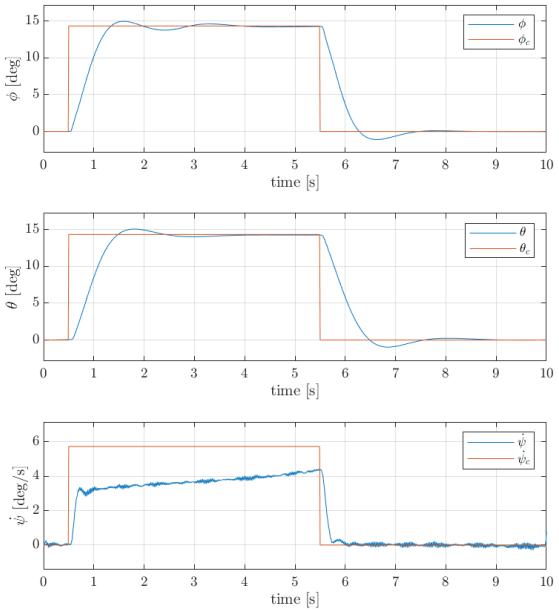

Figure 13: Step response of the attitude controller in wing-borne flight $v \approx 7\,\mathrm{m/s}$ (simulation)

not reach the commanded step within five seconds, whereas for the return of the commanded yaw rate to $0\,^\circ/\mathrm{s}$ a fast response behaviour with a rise time of $t_r = 0.25\,\mathrm{s}$ is observed. This lack in response also occurs in the angular acceleration $\dot{r}$, suggesting that a yawing moment exists, that counteracts the commanded angular acceleration.

Since the step in $\dot{\Psi}$ is isolated and does not include a command in ϕ for a coordinated turn, a slip angle β builds up, see Figure 14.

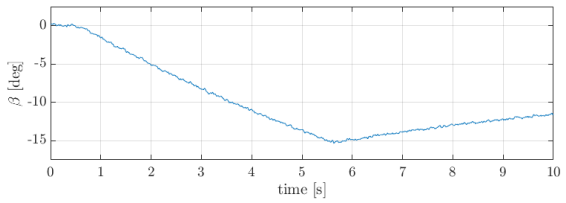

Figure 14: Build-up of a slip angle through a commanded yaw motion (simulation)

By approximating the vertical stabiliser with a finite flat plate of area S_v, aspect ratio Λ_v and a mean lever arm l_v to the aircraft's centre of gravity, the temporal change of yaw moment can be expressed by Equation 10 [13].

$$\frac{\partial N(\dot{\beta})}{\partial t} = \frac{\rho}{2} v^2 \cdot S_v \cdot 2\pi \cdot \frac{\Lambda_v}{\Lambda_v + 2} \cdot \dot{\beta} \cdot l_v \qquad (10)$$

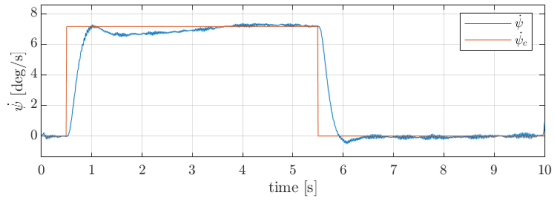

Figure 15: Command response of the yaw rate with adjusted mass properties (simulation)

An evaluation of this Equation shows that the change of yaw moment caused by the change of the slip angle is of the same order as the controller-commanded change of torque for overcoming the aircraft's mass inertia. If the mass properties of Idefix are adjusted to match Maverix's ratio of mass inertia and aerodynamic damping, the response behaviour changes, as shown in Figure 15. This response behaviour fits the command significantly better, which supports the idea that the building-up damping effect of the vertical stabiliser is responsible for the observed lack in response. While neglecting this effect does not impact the command response for Maverix, it does for Idefix. To consider this effect in the controller, the slip-angle has to be determined continuously, which is accompanied by more measurement effort. However, flight states with high slip-angles are rarely required and Idefix's yaw response behaviour while reducing the slip angle is sufficiently fast. Therefore, a special consideration of this effect is not implemented.

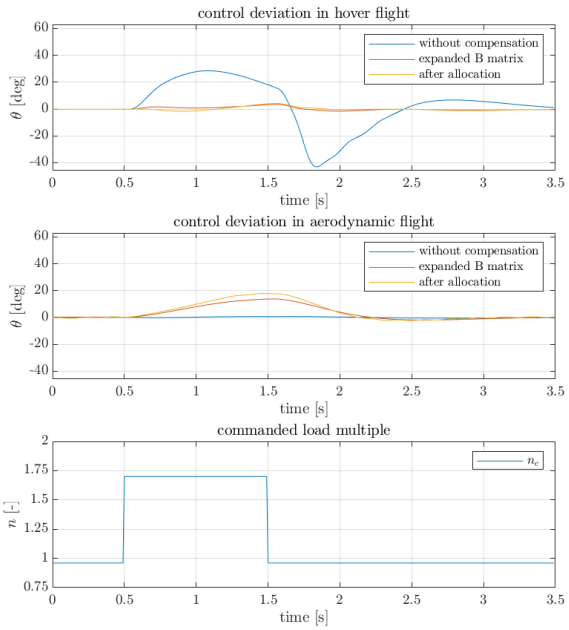

Figure 16: Pitch angle deviation (simulation)

The compenzation of the thrust-induced pitch moment introduced in Section 3.1 and 3.2 is investigated through the response of the pitch angle to commanded load multiples. Figure 16 shows a significant improvement in the control error in hover flight compared to that of the uncompensated case with a reduction of deviation from $40\,^\circ$ to less than $5\,^\circ$. Yet in wing-borne flight, a worsening of the control deviation is observed.

This behaviour can be ascribed to the interaction of the slip stream behind the main motors with the main wing. The inflow downstream the propeller plane is higher than the aircraft's airspeed and thus generates more lift. Figure 17 shows the kinematic correlation between both the additional lift F_{add} and the lever arm h_{add} and the tilt angle σ as well as the geometric parameters of the aircraft x_{tilt} and z_{tilt}. This interaction results in an additional pitch moment $M_{A,add}$, see Equation 11,12 and 13.

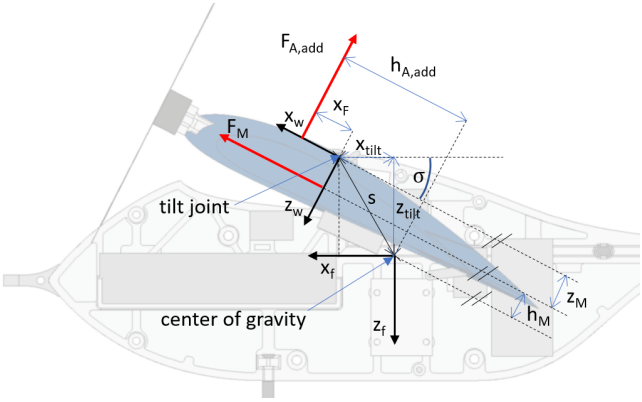

Figure 17: Kinematic correlation of the additional lift induced by the main motors

$$M_{A,add} = F_{A,add} \cdot h_{A,add} \tag{11}$$

$$h_{A,add} = \cos(90^\circ - \arctan\left(\left|\frac{x_{tilt}}{z_{tilt}}\right|\right) - \sigma) \cdot s + x_F \tag{12}$$

$$s = \sqrt{x_{tilt}^2 + z_{tilt}^2} \tag{13}$$

Particularly noteworthy is the moment's change of sign at a tilt angle of $\sigma = 50\,^\circ$. This change means that the pitch moment induced by motor thrust is amplified in a range of $50\,^\circ < \sigma < 90\,^\circ$ and reduced in a range of $0\,^\circ < \sigma < 50\,^\circ$, with a complete cancellation at $\sigma = 50\,^\circ$. Even though it is easy to determine the direction of this moment, the quantification is challenging due to uncertainties in the location of the centre of pressure and consequently the lever arm $h_{A,add}$ as well as the amount of additional force $F_{A,add}$.

To minimise the interaction of these effects without conducting additional wind tunnel experiments, the pitch compenzation is only applied in the tilt angle range of $50\,^\circ < \sigma < 90\,^\circ$, where both effects have the same sign.

4.2 *Free Flight*

Free flights with Idefix show that in hover flight the attitude angle accurately follows the commanded changes and rarely exceeds a deviation of more than 2 °, see Figure 18.

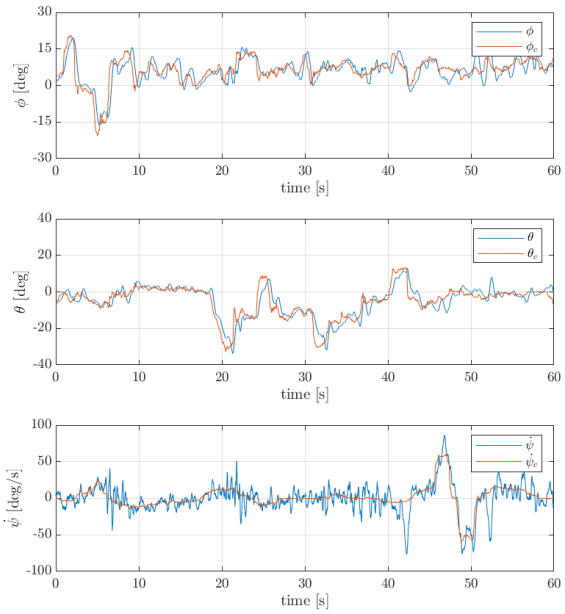

Figure 18: Command response of the attitude controller in hover flight (free flight)

Also in wing-borne flight, a well fitting command response is observed, see Figure 19. This includes yaw rates of up to $\dot{\Psi} = 40\,°/s$ during coordinated turns, which confirms the legitimacy of the previously described negligence of the yaw moment caused by the build-up of a slip angle. Only during turns a control deviation of up to 5 ° is observed, which can be explained by cross flow due to imperfect turns as well as harsh wind conditions on this particular flight.

For the pitch compensation, only flight tests in hover flight are conducted due to the argumentation in Section 4.1, see Figure 20 - 22. These include attitude control without the main motor pitch compensation, compensation with an extended control ability matrix and compensation with consideration as a disturbing effect.

The changes in the load factor are manually commanded and therefore do not represent real steps. To allow comparability with the simulation results, the load factor signals used in the free flights are also run through the simulation used in Chapter 4.1. It is observed that in all cases the real deviation in pitch angle exceeds the simulated deviation, which may be due to the differences between the real aircraft and the simulation. Even though the simulation shows similar results for both compensations, the smallest deviation in the pitch angle during free flight is yielded with compensation through

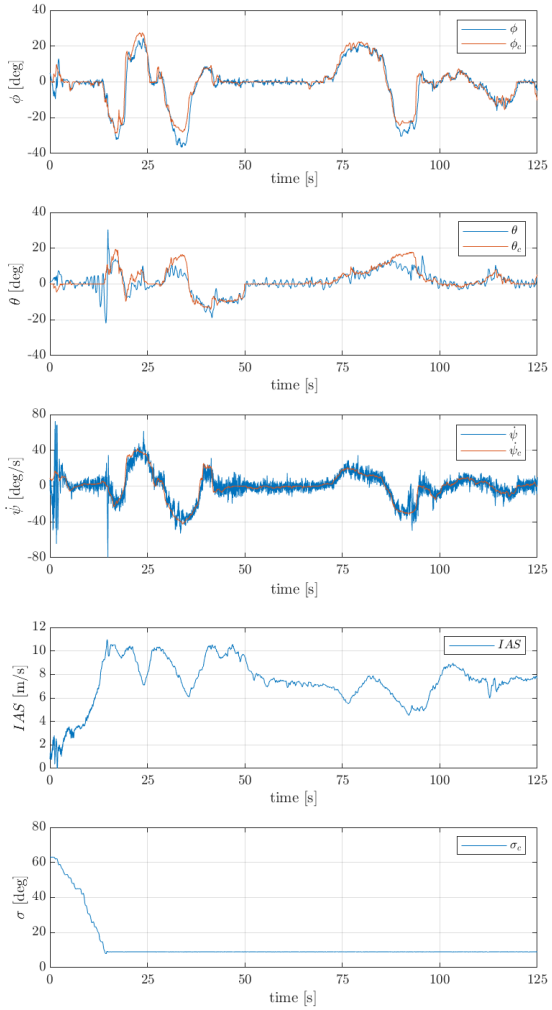

Figure 19: Command response of the attitude controller in wing-borne flight (free flight)

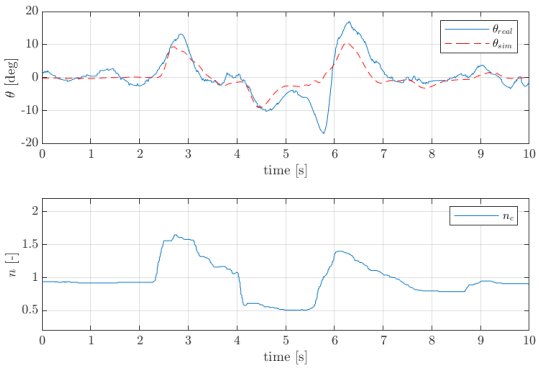

Figure 20: Change of pitch angle without pitch compensation (free flight)

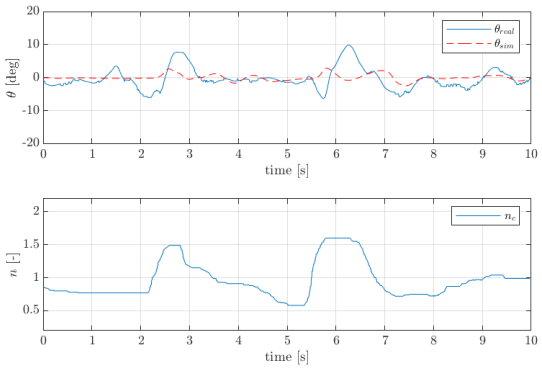

Figure 21: Compensation with extended control ability matrix (free flight)

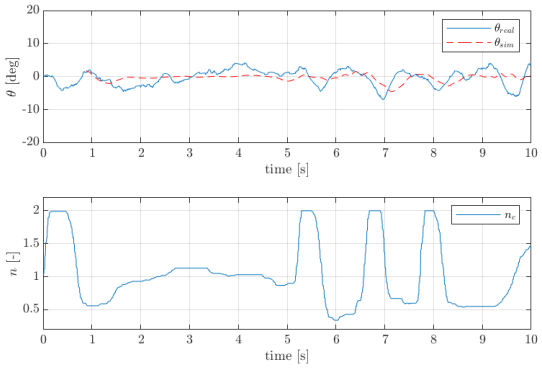

Figure 22: Compensation through consideration as disturbing effect (free flight)

consideration as a disturbing effect. However, as described in Section 4.1, this avoids finding an optimum solution with the allocator and therefore should be used as a reference for further optimization of the allocator.

4.3 Flight performance

All requirements for flight performance set in chapter 2 could be fulfilled for Idefix, as shown in the take-off ready configuration in Figure 23. These include a maximum flight duration of 5 min in hover flight and up to 10 min in wing-borne flight. In stationary horizontal wing-borne flight, an airspeed of $v = 6\,\mathrm{m/s}$ could be achieved at a pitch angle of $\theta = 0\,°$, see Figure 24. Though this already satisfies the requirement, even lower airspeeds in horizontal flight can be achieved at higher angles of attack.

Figure 23: Take-off ready Idefix

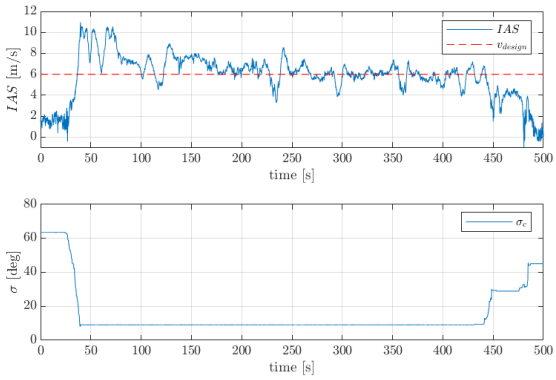

Figure 24: Air speed during free flight

5 Conclusion

In this work the miniaturization of a tiltwing aircraft was conducted. Through consequent lightweight design, the wingspan could be reduced by 66 % and the take-off weight by more than 90 % compared to Maverix, resulting in a take-off weight of $m = 175\,\mathrm{g}$. Special challenges resulting from the miniaturization, such as electromagnetic interference between electronic components due to the small installation space, were identified and solved constructional.

An attitude controller based on the concept of INDI was implemented with focus on expanding the modelling of the main motor's control ability and its implementation in the controller. This was necessary due to the aircraft's rear-positioned centre of gravity and thus the main motors' noticeable pitch ability. In slip flight, damping aerodynamic effects of the vertical stabiliser, which were negligible for Maverix, were identified and quantified for Idefix.

Both the aircraft and the controller were validated in simulations and flight tests and showed stable flight behaviour in both hover and wing-borne flight. With respect to the TLARs, all requirements, including a minimal flight duration of $t = 5\,\mathrm{min}$ and a minimal flight speed of $v = 6\,\mathrm{m/s}$, were fulfilled.

Future work will concentrate on finding a solution for the aircraft's position determination, which complies with the requirements for fully automated flight in GPS-denied areas and improving flight behaviour, especially during the transition from hover to wing-borne flight.

REFERENCES

[1] Domenica Costantino, Maria Giuseppa Angelini, and Gabriele Vozza. The engineering and assembly of a low cost UAV. In *2015 IEEE Metrology for Aerospace (MetroAeroSpace)*, pages 351–355, 2015.

[2] Mostafa Hassanalian, Hamed Khaki, and Mehrdad Khosravi. A new method for design of fixed wing micro air vehicle. *Proceedings of the Institution of Mechanical Engineers, Part G: Journal of Aerospace Engineering*, 229(5):837–850, 2015.

[3] G. C.H.E. De Croon, M. A. Groen, C. De Wagter, B. Remes, R. Ruijsink, and B. W. Van Oudheusden. Design, aerodynamics and autonomy of the DelFly. *Bioinspiration and Biomimetics*, 7(2), 2012.

[4] FSD Homepage - RWTH Aachen University `https://www.fsd.rwth-aachen.de/cms/fsd/Forschung/~mhauu/Fluggeraete/?lidx=1`. Accessed: 2022-08-01.

[5] Paul M. Rothhaar, Patrick C. Murphy, Barton J. Bacon, Irene M. Gregory, Jared A. Grauer, Ronald C. Busan, and Mark A. Croom. NASA langley distributed propulsion VTOL tilt-wing aircraft testing, modeling, simulation, control, and flight test development. *AIAA AVIATION 2014 -14th AIAA Aviation Technology, Integration, and Operations Conference*, pages 1–14, 2014.

[6] Fabian Binz. Robust, Fault-Tolerant Control of Aircraft with Hovering Capability, 2020.

[7] P Hartmann, M Schütt, and D Moormann. Vollständigen Flugbereich Eines Kippflügelflugzeuges. *Deutscher Luft- und Raumfahrtkongress 2014 DocumentID: 340131*, pages 1–9, 2014.

[8] YSHIELD GmbH & Co KG. Electromagnetic Shielding Fleece `https://www.yshield.com/en/artikel_pdf/item/416/variation/1389/`. Accessed: 2022-08-01.

[9] YSHIELD GmbH & Co KG. Electromagnetic Shielding Fleece - Expert report of RF transmission attenuation `https://pdf.yshield.com/pdf/db/EXPERTREPORT-YSHIELD-HNV100.pdf`. Accessed: 2022-08-01.

[10] A Deperrois. About XFLR5 calculations and experimental measurements, 2009.

[11] Philipp Hartmann. Predictive Flight Path Control for Tilt-Wing Aircraft, 2017.

[12] Ingmar Buchweitz. Flugzeugentwurf am Beispiel eines ausgeführten Flugzeugs, 2002.

[13] F. Binz, T. Islam, and D. Moormann. Attitude control of tiltwing aircraft using a wing-fixed coordinate system and incremental nonlinear dynamic inversion. *International Journal of Micro Air Vehicles*, 11, 2019.

[14] Erik-jan Van Kampen. Incremental backstepping for robust nonlinear flight control Incremental Backstepping for Robust Nonlinear Flight Control, 2016.

[15] Ewoud J.J. Smeur, Qiping Chu, and Guido C.H.E. De Croon. Adaptive incremental nonlinear dynamic inversion for attitude control of micro air vehicles. *Journal of Guidance, Control, and Dynamics*, 39(3):450–461, 2016.

[16] João Carlos Alves Barata and Mahir Saleh Hussein. The Moore-Penrose Pseudoinverse: A Tutorial Review of the Theory. *Brazilian Journal of Physics*, 42(1-2):146–165, 2012.